ADVANCED MATERIALS

DOI: 10.1002/adma.200702768

Oriented TiO_2 Nanostructured Pillar Arrays: Synthesis and Characterization**

By *Federico Cesano, Serena Bertarione, Alessandro Damin, Giovanni Agostini, Sandro Usseglio, Jenny G. Vitillo, Carlo Lamberti, Giuseppe Spoto, Domenica Scarano,* and *Adriano Zecchina**

TiO_2 with tailored porosity, particle size, and shape in the nanometer range is attracting a lot of attention because of its potential use in photocatalysis and energy conversion. As far as photocatalysis applications are concerned, the use of high surface area TiO_2 as a photocatalyst for pollutant degradation and for water splitting is of particular interest.[1–7] The presence of bulk defects and grain boundary barriers — associated with the small dimensions of the particles, recombination of electrons, and holes generated by band-gap excitation — is limiting the photoconversion efficiency.[8–10]

To improve charge separation and the associated catalytic efficiency, researchers have essentially followed two strategies. The first centers on tailoring of the size, shape, and three-dimensional organization of TiO_2 particles[1,2,11,12] or of Ti–O–Ti wires with semiconductor character.[5,13–16] The second strategy focuses on improving the photocatalytic properties: i) by incorporating metal cations and anions (mainly nitrogen, sulphur, iodine, and other elements) into the bulk;[6,14,17–23] ii) by supporting metal particles (mainly Au, Ag, Pt, Ni).[1,3,24–31]

Interesting results are obtained when the two above-mentioned research directions are combined to benefit from the sum of their advantages.[32]

Several strategies have been adopted for the development of energy conversion applications in solar cells.[1,3,33–36] Among them, the use of dye-sensitized TiO_2 nanostructures has an outstanding reputation and both experimental and theoretical evaluations of the efficiency-limiting factors have been identified.[33,37,38] Recently, it has been shown that the use of ordered arrays of TiO_2 nanostructures (either pure, such as nanotubes, nanowires, and nanorods[39–41] or TiO_2-based architectures,[15,42,43] which replace the traditional nanoparticle film) can improve the efficiency.[9,34,40,43–49] Moreover, it is evident from recent literature data[1,3,9,44,50] that the innovative synthesis of TiO_2 particle arrays, either pure or anchored to conducting substrates, plays a leading role in both photocatalysis and energy conversion applications.

In this paper, we describe a new method for the synthesis of parallelly aligned TiO_2 micropillars, either pure or fixed to a rigid carbon support. Accurate characterization shows that, depending upon the synthesis conditions, the micropillars constitute of partially cemented pure anatase or a mixture of coexisting anatase and rutile particles with a diameter in the 10–20 nm range. The obtained materials combine high surface areas ($\sim 60\,m^2/g$), controlled crystal structures, and an unprecedented architecture, which guarantees good interparticle contacts. We believe that these three-dimensionally organized, parallelly oriented structures can offer important advantages in dye-sensitized solar cell technology, because it is known that elongated structures with high crystalline character show increased efficiency for electron transfer and reduced ''hopping charge'' across the nanoparticle grain boundaries.[8,9]

TiO_2/carbon composites and TiO_2 pillars were prepared following the steps of the procedure outlined in Scheme 1. It will be shown below that Route 1 leads to the formation of a homogeneous film formed by parallel TiO_2 pillars implanted on the carbonaceous support (TiO_2/C composite), whereas Route 2 leads to pure elongated TiO_2 pillars that preserve the parallel orientation. The carbonaceous foils prepared following Route 1 show a modest conductivity ($\sim 10^{-4}$ S/cm). In contrast, the conductivity properties of the support increase rapidly, up to ~ 0.3 S/cm (800 °C), after successive thermal treatment under a flow of pure N_2, which favors partial graphitization of the carbon.

Samples obtained following Route 1. Scanning electron microscopy (SEM) images of the final material obtained following Route 1 (TiO_2/C) are shown in Figure 1a–c. In Figure 1a, the top view of the foil surface is shown, while in Figure 1b and 1c, lateral views taken at the edge of the foil at different magnification levels are reported. From these images it can be inferred that TiO_2 emerging from the carbonaceous phase forms elongated micropillars (Fig. 1b) with rounded and apparently smooth caps (Fig. 1c). From the images of Figure 1b and 1c it was determined that the average diameter of the pillar

[*] Prof. A. Zecchina, Dr. F. Cesano, Dr. S. Bertarione, Dr. A. Damin, Dr. G. Agostini, Dr. S. Usseglio, Dr. J. G. Vitillo, Prof. C. Lamberti, Prof. G. Spoto, Prof. D. Scarano
Department of Inorganic, Physical, and Materials Chemistry
NIS (Nanostructured Interfaces and Surfaces) Centre of Excellence and INSTM Centro di Riferimento
University of Torino
Via P. Giuria, 7, 10125 Torino (Italy)
E-mail: adriano.zecchina@unito.it

[**] The authors would like to thank MIUR, INSTM Consorzio, NANOMAT Project and the Regione Piemonte Research Program (Sistemi a base di carbonio nanostrutturato per applicazioni industriali -D37) for financial support, Dr. Micaela Castellino for helping with conductivity measurements. Supporting Information is available online from Wiley InterScience or from the author.

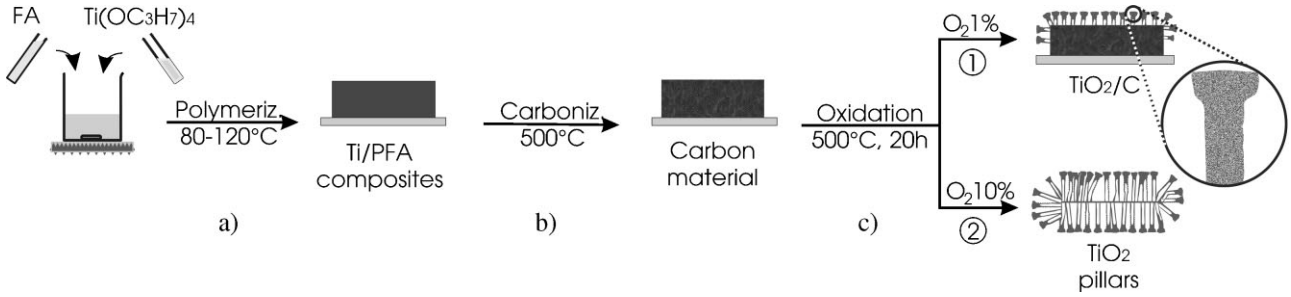

Scheme 1. Preparation steps of TiO_2/C composites and of pure TiO_2 pillars: a) acid-catalyzed polymerization of the furfuryl alcohol (FA) and Ti isopropoxide ($Ti(OC_3H_7)_4$) solution, under mild conditions (80–120 °C), with formation of a Ti/PFA composite; b) pyrolysis step under N_2 flow at 500 °C, with formation of a carbon composite; c) oxidation of the carbonaceous composite under N_2/O_2 gas mixture at 500 °C. Route 1 (1% O_2) corresponds to the oxidation of the external surface layers and formation of TiO_2 pillars implanted on the carbonaceous matrix (TiO_2/C composite). Route 2 (10% O_2) corresponds to the total oxidation of the carbon matrix with formation of pure TiO_2 pillars.

heads and stems were in the 6–8 μm and 5–6 μm range, respectively, while the length of the emerging part of the pillars was about 18–20 μm (see Fig. 1b). These micropillars were not significantly damaged by subsequent manipulation for SEM analysis and were partially embedded in the carbon matrix. This was confirmed by the results shown in Figure 1b and 1c (where it can be seen clearly that the pillars are emerging perpendicularly from the underlying support) and by energy dispersive X-Ray (EDX) data shown in Figure 1d, where the local composition of two selected regions of the pillars of Figure 1b is reported (i.e., the top section of the pillars (black-striped area) and at the base of the pillars (white-striped area)). EDX analysis showed that titanium and oxygen were the dominant elements present on the cap, while the carbon signal became very important at the base of the pillars.

Similar results were obtained from micro-Raman and X-ray diffraction (XRD) experiments. In particular, the micro-Raman spectra (Fig. 1e, black curve), taken on the caps of the

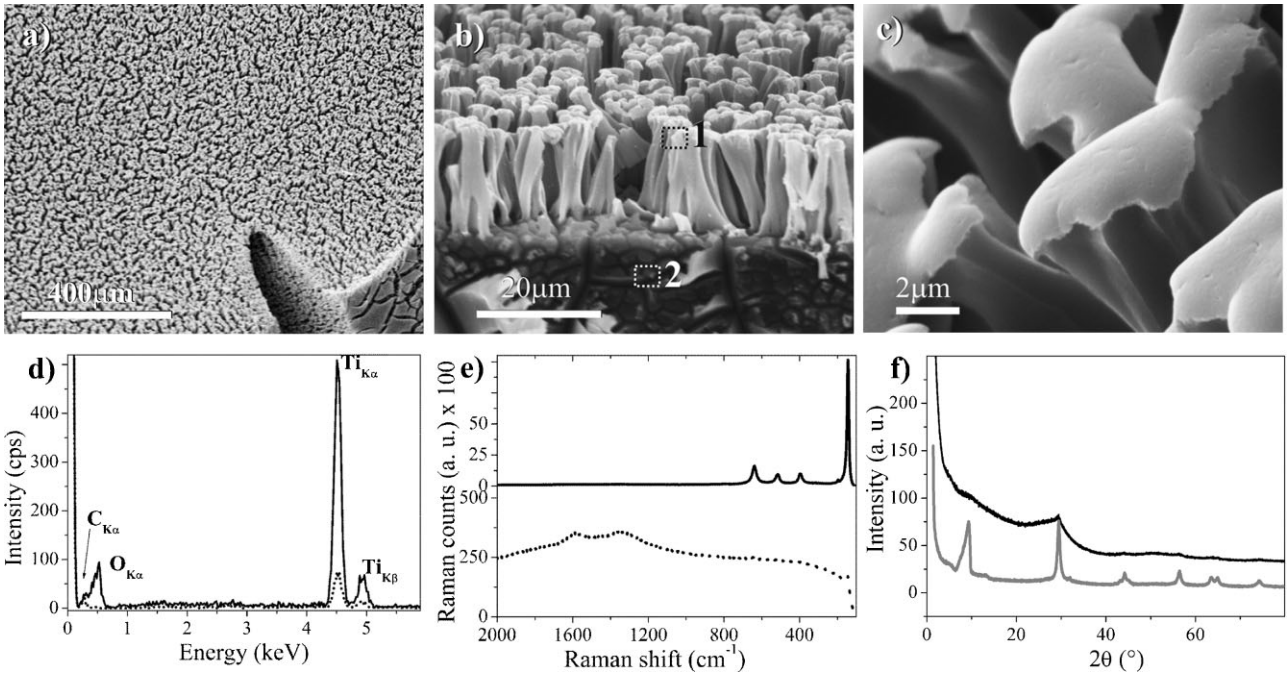

Figure 1. Morphology, chemical and structural analysis of the samples obtained from Route 1: a) SEM image of the TiO_2/C composite at low magnification. b) SEM image on top view of the edge of a monolith. From this image the occurrence of micropillars that protrude from the support is illustrated. c) Enlarged SEM image of the pillar caps. d) EDX and e) Raman spectra taken on the two selected areas: on the top (black curve) and at the basis (dotted curve) of the pillar arrays. f) XRD patterns taken at grazing angle on the monolith (gray curve) and on the same powdered material (black curve); from these images it is clear that the two phases, anatase TiO_2 and amorphous carbon, are coexisting.

ADVANCED MATERIALS

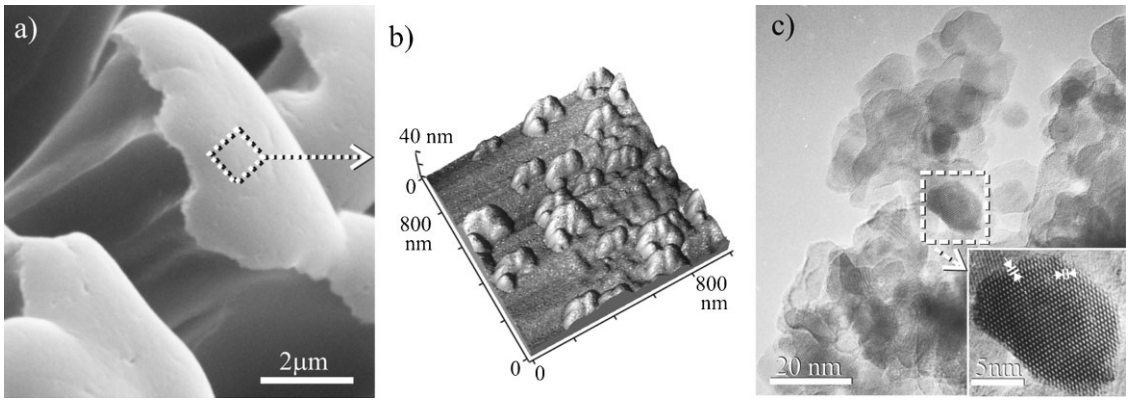

Figure 2. Morphology and microstructure of the pillars protruding from the carbon support obtained from Route 1: a) SEM enlarged image of an apparently smooth and rounded upper surface of a TiO_2 pillar; b) a selected area on a pillar cap as imaged by AFM. In this picture, agglomerates of nanoparticles of 200–300 nm, are evidenced; c) TEM image of a region on the sample. In the inset, a HRTEM enlarged view of a selected particle in c) 10–20 nm in size is highlighted. Two families of interference fringes are simultaneously observed, whose spacings (3.50 and 3.51 Å, respectively) are associated with the (101) interplanar distance of anatase.

micropillars, showed the typical six Raman modes of the TiO_2 anatase phase ($A_{1g} + 2B_{1g} + 3E_g$) (peaks at 638.8 cm^{-1}(E_g), 516.9 cm^{-1} (A_{1g}, B_{1g}), 396.7 cm^{-1} (B_{1g}), 197.5 cm^{-1} (E_g), and 143.8 cm^{-1} (E_g)). It is worth noticing that the peak position (in particular the 144 cm^{-1} E_g mode) and the peak width (i.e., full width at half maximum (FWHM)) are in agreement with literature data reported for small anatase nanocrystals).[1] In contrast, the spectra taken at the base of the pillars (Fig. 1e, dotted curve) are dominated by the G and D Raman modes of the turbostratic carbon phase (peaks at 1580 cm^{-1} and 1350 cm^{-1}),[51–53] even if a small contribution of the anatase Raman peaks is detected.

The same conclusions can be drawn from XRD experiments taken on the as-obtained monolith (to maximize the contribution of the surface layers, Fig. 1f, gray curve) and on the powdered material (Fig. 1f, black curve), where the contribution of the underlying carbonaceous support becomes predominant. The XRD pattern of the monolith sample taken at the grazing incidence angle clearly shows that the external layers are dominated by crystalline anatase peaks, while that taken of the powdered sample is dominated by two broad signals of the carbonaceous support (low-intensity bands covering the $2\theta \cong 20–35^\circ$ and $2\theta \cong 48–52^\circ$ ranges, which are associated with the out-of-plane and in-plane low-range ordering of the graphene sheet structure), and a sharp signal at $2\theta \cong 29.4^\circ$ attributable to the (101) anatase diffraction peak.

Scherrer's equation was used to calculate a mean crystal size of about 18 nm from the (101) diffraction peak of anatase at $2\theta \cong 29.4^\circ$ (gray pattern). The sharp diffraction peak ($2\theta \cong 9.7^\circ$) of the pattern taken from the monolith at grazing incidence suggests that the external layers may be mesoporous (vide infra) and that this porosity shows some structural regularity.

The SEM images of the TiO_2/C composite provided information on the gross morphology of the TiO_2 particles, but nothing could be inferred about the nanometric and sub-nanometric structure of the pillars.

To obtain more information on the (sub-)nanometric structure of the pillars, two types of experiments were performed: atomic force microscopy (AFM) was used in non-contact mode to investigate the structure of the cap of the pillars (shown in Fig. 2a). A typical 3D AFM image is reported in Fig. 2b. Secondly, high-resolution transmission electron microscopy (HRTEM) was performed on the nanoparticles obtained from the pillars; typical results are shown in Fig. 2c. From the 3D non-contact AFM image (Fig. 2b) it was concluded that the surface of the pillars was not smooth; the surface was populated by "hills" of irregular shape of about 300 nm in size, which emerged from a flat and apparently smooth background. From the XRD results it was evident that these hills constituted of aggregates of smaller particles.

In this respect, HRTEM analysis was more informative, because Figure 2c clearly shows that the pillars on the TiO_2/C system constituted of anatase particles with a diameter in the 15 ± 5 nm range. The results shown in Figure 2c agreed closely with the XRD results (which indicated a mean crystal size of about 19 nm). These particles were partially cemented as a result of the sintering treatment.

The obtained discrepancy between the particle size in the AFM images and that observed by TEM/XRD can be explained as follows: i) the discrepancy is in agreement with the difference in resolution: AFM (5–10 nm) is imaging only aggregates, whereas TEM (0.25 nm) reveals the single constituents of the aggregates[54]; ii) the same holds true when AFM and XRD results are compared.

BET measurements (Table 1) performed on this system gave a surface area of ~11 m^2/g (see also Fig. 5a). On basis of the particle dimensions, the surface area of the emerging TiO_2 pillars is expected to be higher, but the specific surface area of the TiO_2 phase cannot be determined with sufficient confidence because of the low thickness of the emerging

Table 1. Textural properties of the TiO_2/C composites.

	S_{BET} [m^2/g]	S_{micro}[a] [m^2/g]	S_{meso}[a] [m^2/g]	S_{meso}[b] [m^2/g]	V_{pore}[c] [cm^3/g]
O_2 1% (v/v)	11	9	n.a.	6	0.008
O_2 10% (v/v)	56	0	37	57	0.104

[a]Estimated using the t-plot method (Harkins and Jura thickness curve). [b]Estimated using the BJH adsorption branch of the isotherm (Kruk–Jaroniec–Sayari thickness curve, Faas correction). [c]Single-point total pore volume at $P/P_0 \cong 0.98$.

TiO_2 pillars and because of the not negligible contribution of the underlying compact carbon support.

Samples obtained following Route 2. SEM images of the material obtained under stronger oxidizing conditions (Route 2, Scheme 1) are shown in Fig. 3a–c. In Fig. 3a, the top view of the material shows a carpet of micropillars similar to that illustrated in Fig. 1, but some differences are nevertheless evident. The lateral view shown in Fig. 3b shows a double array of parallelly oriented TiO_2 micropillars forming a thin foil of about 0.2 mm thick (10 mm × 10 mm in size) without any trace of carbonaceous phase. The double layer is a consequence of the oxidation process, which occurs simultaneously and in the same way on the two parallel faces of the monolith (see Scheme 1). This means that the carbonaceous phase will be consumed totally by combustion under strong oxidation conditions (10% O_2). Enlarged SEM images (Fig. 3b and 3c) show that the average dimensions of the pillar heads (which are definitely more irregularly shaped) and stems can be estimated to be in the 5–10 μm and 25–30 μm range, respectively. From Figure 3c, it is also possible to observe that the pillars often have branched terminations with multiple heads (whose individual size is consequently smaller than that of the pillars observed under less oxidizing conditions). We anticipate that this morphological difference is likely to be related to temperature differences. In fact, it is quite conceivable that the local temperature of the composite foil during total oxidation can be higher than that of the surrounding furnace. In Figure 3d, EDX analysis on an extended region of the sample is shown; this testifies the presence of a chemically homogeneous phase, mainly formed by titanium and oxygen.

Further insights on the nature of the formed TiO_2 phases were obtained from the Raman spectra. The Raman spectrum (Fig. 3e) shows that besides the peaks at 635.6 cm^{-1}, 515.8 cm^{-1}, 395.5 cm^{-1}, 196.3 cm^{-1}, and 142.6 cm^{-1}, associated with the anatase phase and observed at slightly lower frequencies than the previous sample (see Fig. 1e). Moreover,

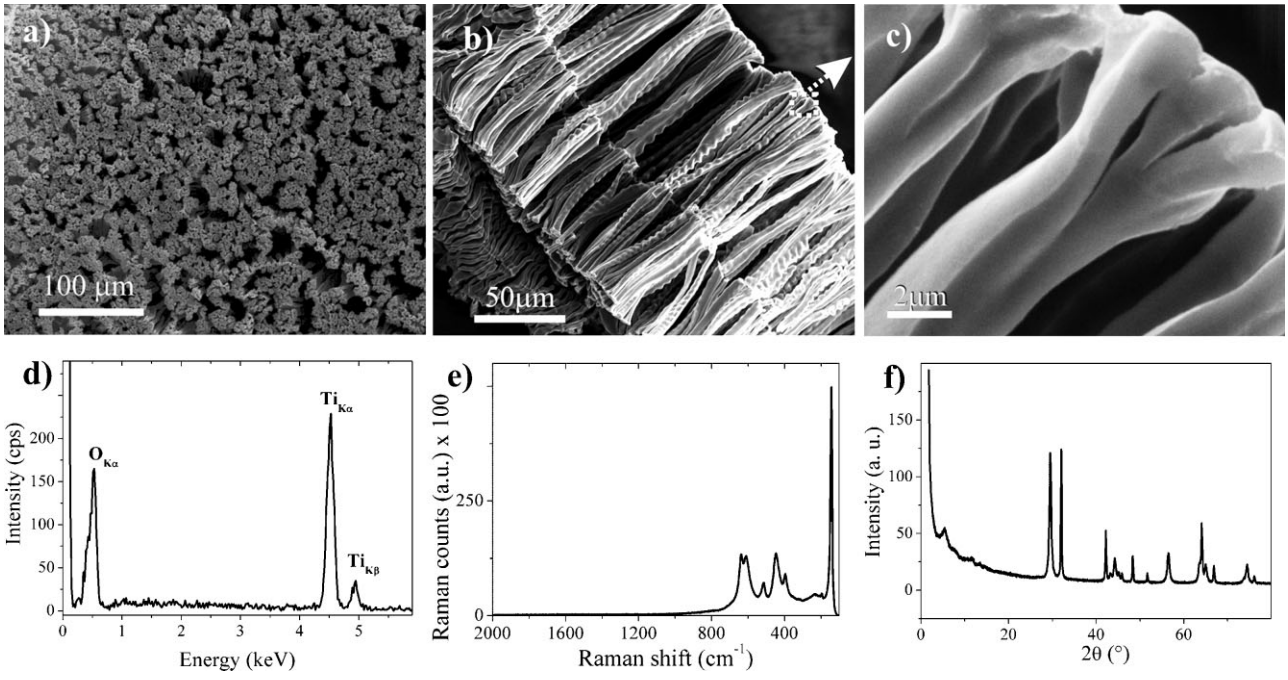

Figure 3. Morphology, chemical and structural analyses of the sample obtained from Route 2: a) on top and b) lateral view SEM images of the TiO_2 pillar arrays; c) SEM enlarged view of a TiO_2 pillar branched termination of b). From these images, the occurrence of an ordered bi-dimensional array of micropillars, is clearly evidenced. d) EDX, e) Raman spectra and f) XRD pattern taken on the sample totally oxidized. It is evident that the formed micropillars are constituted of coexisting phases of anatase and rutile.

ADVANCED MATERIALS

the peaks at 608.8 cm^{-1} (A_{1g}), 446.9 cm^{-1} (E_g) and 232.96 cm^{-1}, associated with rutile phase can be observed. This means that both TiO_2 phases coexist under the applied experimental conditions. Further support to the coexistence of both anatase and rutile phases can be found in the XRD diffraction pattern shown in Figure 3f. In this figure, intense and narrow diffraction peaks of both the antase and rutile phase are observed simultaneously: the peaks at $2\theta \cong 29.4^\circ$ (101), $2\theta \cong 44.2^\circ$ (004), $2\theta \cong 56.4^\circ$ (200), $2\theta \cong 63.5^\circ$ (105), $2\theta \cong 65.0^\circ$ (211), and $2\theta \cong 74.5^\circ$ (204) were attributed to the anatase phase, and those at $2\theta \cong 32.0^\circ$ (110), $2\theta \cong 42.1^\circ$ (101), $2\theta \cong 48.3^\circ$ (111), $2\theta \cong 64.1^\circ$ (211), $2\theta \cong 66.9^\circ$ (220), $2\theta \cong 76.1^\circ$ (310) were associated with the rutile phase.

By applying Scherrer's equation to the $2\theta \cong 29.4^\circ$ (101) anatase and $2\theta \cong 32.0^\circ$ (110) rutile diffraction peak, a mean crystal size of about 22 and 57 nm was calculated for the anatase and rutile phases, respectively.

We excluded the presence of titanate compounds, because both the low-angle XRD peaks ($2\theta \cong 8$–12° range, $d_{hkl} = 7 \div 10$ Å)[55–57] and the typical Raman features of these compounds were absent.[55,56]

SEM, AFM, and TEM measurements confirmed that samples prepared following Route 2 were completely constituted of cemented nanocrystals and that the pillars had a robust character (i.e., were not destroyed by manipulation)(see also Supporting Information). In Figure 4a an SEM image of an isolated pillar is shown. Figure 4b shows an AFM image (obtained in 3D non-contact mode) of a selected area on the pillar side. For the sake of brevity, this figure only shows the result concerning a selected area on the pillar stem; it demonstrates (similar to the results in Fig. 2b) that the surface is rough because of the presence of small agglomerates of nanoparticles ranging 50–150 nm in size. From the TEM images (Fig. 4c), more accurate information is obtained about the degree of aggregation and the dimensions of the single particles. In particular, this figure reveals that the sample is made of dense and compact aggregates of small nanocrystals, whose dimensions were estimated in the range of 20 ± 5 nm. It can be noticed that the thinner particles show the presence of interference fringes, whose spacing is associated with the (110) interplanar distance of the rutile phase. From this image and from others (not reported here for the sake of brevity), which all explored small selected areas, we can neither rule out the simultaneous presence of the anatase phase, as previously shown by XRD analyses, nor the presence of other diffraction planes associated with different TiO_2 phases.

On basis of these morphological results, we can state that the arrays of TiO_2 micropillars are produced by self-assembly of nanoporous TiO_2 anatase and rutile particles. As far as the surface area and porosity are concerned, the results of the volumetric measurements are summarized in Table 1, whereas the N_2 adsorption–desorption isotherms of the samples coming from Route 1 and Route 2 are shown in Figure 5a. As the oxidation is consuming the carbon phase, the specific surface area increases up to 60 m^2/g and the N_2-adsorption isotherms approaches the typical shape characteristic of mesoporous adsorbents. Moreover, the absence of a plateau after the hysteresis loop represents an indication that the contribution of the external surface area is small (see Table 1). In Figure 5b the pore distribution of the pure TiO_2 pillar sample, as obtained by DFT analysis (slit geometry), is reported. From this plot, it can be concluded that the fully oxidized sample exhibits a quasi-bimodal pore distribution, with the first narrow peak (FWHM ~10 Å) being centered at 26 Å and the second wider peak (FWHM ~60 Å) at 80 Å. The peak centered at 26 Å confirms the presence of pores about 20 Å in diameter, as indicated by the XRD pattern.

The reflectance spectra of TiO_2/C composite and of TiO_2 pillars are compared in Figure 6. From this figure it can be seen that the absorption edge of the TiO_2 pillars obtained following Route 2 is red-shifted compared to that of the TiO_2/C composite. This fact is in agreement with the ascertained

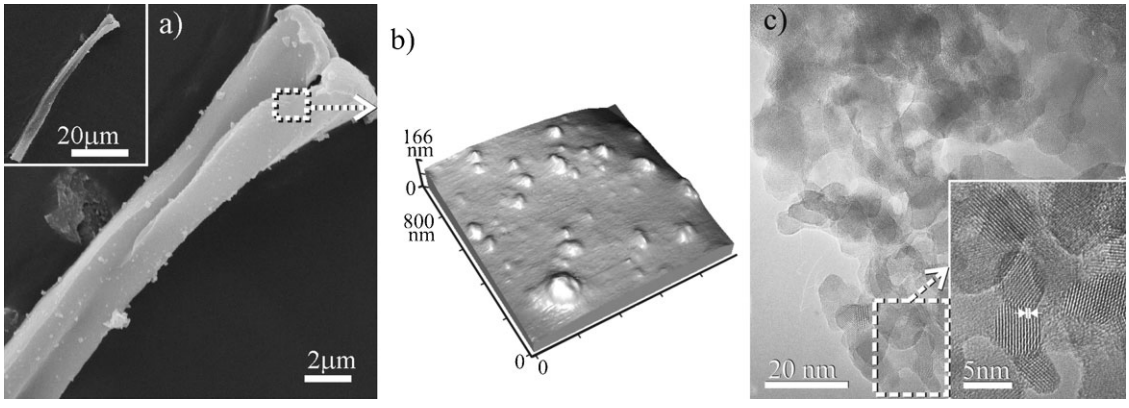

Figure 4. Morphology and microstructure of the sample, obtained from Route 2: a) SEM images of an isolated TiO_2 pillar (single pillars can be obtained by pressing the TiO_2 pillar arrays shown in Fig. 3b); b) selected area on a pillar side, as imaged by AFM. In these figures, the apparently smooth and rounded side surface of the TiO_2 pillar shows a roughness due to the presence of nanoparticle agglomerates of about 50–150 nm range size; c) TEM image of a portion of the sample. In the inset, a HRTEM enlarged view of a selected area of (c) is imaged, where a particle of about 5 nm is exposing interference fringes, whose spacing (3.25 Å) is associated with the (110) interplanar distance of rutile.

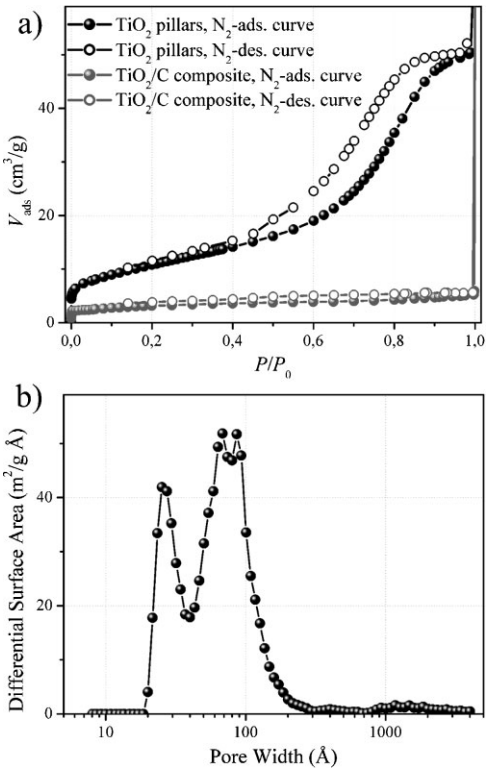

Figure 5. Volumetric results and pore size distribution of TiO_2 pillars as a function of the relative pressure P/P_0. a) 77K N_2 adsorption-desorption isotherms of samples obtained from Route 1 (TiO_2/C composite material, grey curves) and Route 2 (free-standing TiO_2 pillar array, black curves). b) pore size distribution for the pure TiO_2 pillar sample, as obtained from DFT analysis (slit geometry) of the N_2 adsorption data reported in (a); from this figure, a bimodal pore-size distribution (20–40 Å and 40–150 Å, respectively) is evident.

presence of rutile, whose absorption edge is occurring at lower energy than that of anatase. As this shift can also be caused by carbon doping,[58,59] we cannot state a correlation of the obtained results with crystal sizes at this point because we cannot rule out the presence of carbon-doped TiO_2.

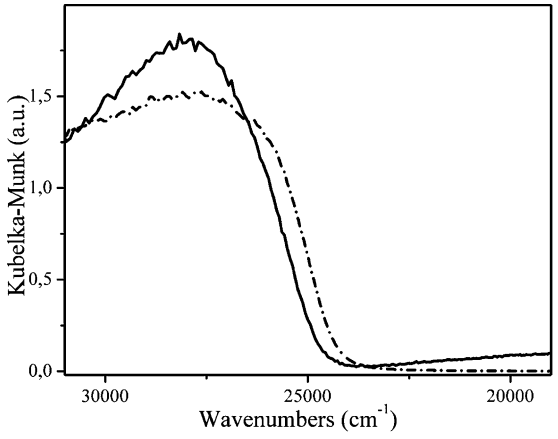

Figure 6. UV-vis reflectance spectra of TiO_2/C composite (solid black curve) and of TiO_2 pillars (dot-dashed black curve).

In conclusion, it can be inferred that the nanostructured and parallelly oriented TiO_2 micropillar arrays, either pure or implanted on a carbon matrix, formed by anatase or a fraction of anatase/rutile nanoparticles, can be obtained from controlled combustion of TiO_2/C composites. Mild oxidation treatment at 500 °C under a flow of N_2 containing 1% of oxygen leads to the formation of parallelly oriented elongated pillars that emerge from a compact amorphous carbon phase. These pillars are mesoporous and constitute of partially cemented anatase particles with diameters in the 10–20 nm range and a surface area of ~60 m^2/g. When the oxidation process is performed under a gas flow containing 10% of O_2, an array of pure parallelly oriented TiO_2 pillars, which constitute of small anatase and rutile nanoparticles, are formed. Pure TiO_2 pillars that constitute of nearly pure anatase phase can be obtained by a further prolonged oxidation process in the presence of 10% oxygen. We believe that the presented synthesis method, which leads to parallelly packed porous pillars with lengths in the μm-range and constituted of cemented anatase and rutile crystals with sizes in the 10–20 nm range, can be useful in photocatalysis and energy conversion applications.

Experimental

A solution of 2-furanmethanol (furfuryl alcohol, (FA)) and Ti isopropoxide (~9% w/w) was prepared at room temperature. The solution was then heated (T = 100–120 °C) to obtain a solid resin (Scheme 1, step a). This resinification step occurs at low temperature because of the catalytic action of Ti(IV), which acts as a Lewis acid [60]. The obtained material (in the form of a foil ~0.2–1 mm thick) was then placed in a quartz tube and the temperature was gradually increased up to 500 °C (heating rate = 5 °C/min) under a flow of 100 mL/min N_2 (Scheme 1, step b). At the end of this step the foil is black and rigid. The carbonaceous composite was then oxidized at 500 °C for 20 h (Scheme 1, step c) following two different procedures. In the first one (Route 1) the gas flow contained approximately 1% O_2, whereas the amount of O_2 was increased to 10% in Route 2. Under mild oxidation conditions (~1% O_2) and the oxidation time not exceeding 12 h, the surface of the composite was oxidized and the advancing oxidation boundary only involved the external layers of the carbonaceous material. On the contrary, oxidation in a gas flow containing 10% O_2 led to total consumption of the carbon matrix. Total combustion was also obtained by exposure to 1% O_2 flow for several days.

The morphology of the sample has been investigated by means of SEM (Leica Stereoscan 420 instrument) equipped with an EDX spectroscopy detector, AFM (Park Scientific Instrument Auto Probe LS), and TEM (Jeol 200EX instrument equipped with a top entry stage, 2.5 Å point resolution). The crystallinity and the phase composition of samples have been estimated by XRD analysis (X-ray diffractometer with Co K_α radiation using a standard Bragg–Brentano geometry) and Raman spectroscopy (Renishaw Raman Microscope with diode laser operating at 785 nm). Diffuse reflectance UV-vis spectra have been recorded directly on the materials at room temperature by means of a Perkin Elmer spectrometer (UV-vis Lambda19) equipped with a diffuse reflectance attachment. N_2 adsorption–desorption experiments have been carried out at 77K (Micromeritics ASAP 2020 instrument) to determine the Brunauer–Emmett–Teller (BET) surface area and micropore volume (t-plot method). Before the surface area determination, the samples were always degassed at 150 °C for 12 h. Temperature-programmed desorption (TPD) analysis (Hyden Catlab) have been performed in bar mode (pressure ranging in the 10^{-6} to 10^{-8}

ADVANCED MATERIALS

Torr range; 1 Torr = 133 Pa) to evaluate the evolution of the volatile species from RT to 800 °C(5 °C/min heating rate) under He gas flow (50 mL/min). Results concerning TPD analysis are reported in the Supporting Information.

Received: November 7, 2007
Revised: February 1, 2008
Published online: July 14, 2008

[1] X. Chen, S. S. Mao, *Chem. Rev.* **2007**, *107*, 2891.
[2] C. Burda, X. B. Chen, R. Narayanan, M. A. El-Sayed, *Chem. Rev.* **2005**, *105*, 1025.
[3] P. V. Kamat, *J. Phys. Chem. C* **2007**, *111*, 2834.
[4] P. Calza, C. Pazè, E. Pelizzetti, A. Zecchina, *Chem. Commun.* **2001**, 2130.
[5] F. X. Llabrés i Xamena, P. Calza, C. Lamberti, C. Prestipino, A. Damin, S. Bordiga, E. Pelizzetti, A. Zecchina, *J. Am. Chem. Soc.* **2003**, *125*, 2264.
[6] S. Usseglio, A. Damin, D. Scarano, S. Bordiga, A. Zecchina, C. Lamberti, *J. Am. Chem. Soc.* **2007**, *129*, 2822.
[7] S. U. M. Khan, M. Al-Shahry, W. B. Ingler, *Science* **2002**, *297*, 2243.
[8] R. O'Hayre, M. Nanu, J. Schoonman, A. Goossens, *J. Phys. Chem. C* **2007**, *111*, 4809.
[9] Y. Suzuki, S. Ngamsinlapasathian, R. Yoshida, S. Yoshikawa, *Cent. Eur. J. Chem.* **2006**, *4*, 476.
[10] C. S. Karthikeyan, H. Wietasch, M. Thelakkat, *Adv. Mater.* **2007**, *19*, 1091.
[11] T. L. Thompson, J. T. Yates, *Top. Catal.* **2005**, *35*, 197.
[12] M. Kitano, M. Takeuchi, M. Matsuoka, J. M. Thomas, M. Anpo, *Chem. Lett.* **2005**, *34*, 616.
[13] S. Usseglio, P. Calza, A. Damin, C. Minero, S. Bordiga, C. Lamberti, E. Pelizzetti, A. Zecchina, *Chem. Mater.* **2006**, *18*, 3412.
[14] M. Alvaro, E. Carbonell, V. Fornes, H. Garcia, *Chem. Phys. Chem.* **2006**, *7*, 200.
[15] P. Atienzar, S. Valencia, A. Corma, H. García, *Chem. Phys. Chem.* **2007**, *8*, 1115.
[16] P. D. Southon, R. F. Howe, *Chem. Mater.* **2002**, *14*, 4209.
[17] H. Wang, J. P. Lewis, *J. Phys. : Condens: Matter* **2006**, *18*, 421.
[18] R. Asahi, T. Morikawa, T. Ohwaki, K. Aoki, Y. Taga, *Science* **2001**, *293*, 269.
[19] T. Ihara, M. Miyoshi, Y. Iriyama, O. Matsumoto, S. Sugihara, *Appl. Catal. B:Environ.* **2003**, *42*, 403.
[20] T. Chiaramonte, L. P. Cardoso, R. V. Gelamo, F. Fabreguette, M. Sacilotti, M. C. Marco de Lucas, L. Imhoff, S. Bourgeois, Y. Kihn, M. J. Casanove, *Appl. Surf. Sci.* **2003**, *212*, 661.
[21] C. Burda, Y. B. Lou, X. B. Chen, A. C. S. Samia, J. Stout, J. L. Gole, *Nano Lett.* **2003**, *3*, 1049.
[22] M. Batzill, E. H. Morales, U. Diebold, *Phys. Rev. Lett.* **2006**, *96*, 026103.
[23] A. Ghicov, J. M. Macak, H. Tsuchiya, J. Kunze, V. Haeublein, L. Frey, P. Schmuki, *Nano Lett.* **2006**, *6*, 1080.
[24] T. G. Schaaff, D. A. Blom, *Nano Lett.* **2002**, *2*, 507.
[25] A. Corma, P. Serna, *Science* **2006**, *313*, 332.
[26] M. S. Chen, D. W. Goodman, *Science* **2004**, *306*, 252.
[27] Y. Ohko, T. Tatsuma, T. Fujii, K. Naoi, C. Niwa, Y. Kubota, A. Fujishima, *Nat. Mater.* **2003**, *2*, 29.
[28] P. D. Cozzoli, R. Comparelli, E. Fanizza, M. L. Curri, A. Agostiano, D. Laub, *J. Am. Chem. Soc.* **2004**, *126*, 3868.
[29] M. J. Uddin, F. Cesano, S. Bertarione, F. Bonino, S. Bordiga, D. Scarano, A. Zecchina, *J. Photochem. Photobiol. A: Chem.* **2008**, *196*, 165.
[30] C. Langhammer, Z. Yuan, I. Zoric, B. Kasemo, *Nano Lett.* **2006**, *6*, 833.
[31] N. R. de Tacconi, J. Carmona, K. Rajeshwar, *J. Phys. Chem. B* **1997**, *101*, 10151.
[32] J. H. Park, S. Kim, A. J. Bard, *Nano Lett.* **2006**, *6*, 24.
[33] M. Gratzel, *J. Photochem. Photobiol. A: Chem.* **2004**, *164*, 3.
[34] G. K. Mor, O. K. Varghese, M. Paulose, K. Shankar, C. A. Grimes, *Sol. Energy Mater. Sol. Cells* **2006**, *90*, 2011.
[35] N. G. Park, K. M. Kim, M. G. Kang, K. S. Ryu, S. H. Chang, Y. J. Shin, *Adv. Mater.* **2005**, *17*, 2349.
[36] N. Robertson, *Angew. Chem. Int. Ed.* **2006**, *45*, 2338.
[37] G. Smestad, C. Bignozzi, R. Argazzi, *Sol. Energy Mater. Sol. Cells* **1994**, *33*, 253.
[38] G. Smestad, *Sol. Energy Mater. Sol. Cells* **1994**, *33*, 254.
[39] J. M. Macak, H. Tsuchiya, L. Taveira, S. Aldabergerova, P. Schmuki, *Angew. Chem. Int. Edit.* **2005**, *44*, 7463.
[40] T. Tachikawa, S. Tojo, M. Fujitsuka, T. Sekino, T. Majima, *J. Phys. Chem. B* **2006**, *110*, 14055.
[41] Y. X. Yin, Z. G. Jin, F. Hou, X. Wang, *J. Am. Ceram. Soc.* **2007**, *90*, 2384.
[42] M. Alvaro, E. Carbonell, P. Atienzar, H. Garcia, *Chem. Phys. Chem.* **2006**, *7*, 1996.
[43] E. Stathatos, P. Lianos, *Adv. Mater.* **2007**, *19*, 3338.
[44] K. Zhu, N. R. Neale, A. Miedaner, A. J. Frank, *Nano Lett.* **2007**, *7*, 69.
[45] G. K. Mor, K. Shankar, M. Paulose, O. K. Varghese, C. A. Grimes, *Nano Lett.* **2006**, *6*, 215.
[46] M. Law, L. E. Greene, J. C. Johnson, R. Saykally, P. D. Yang, *Nat. Mater.* **2005**, *4*, 455.
[47] J. J. Wu, C. C. Yu, *J. Phys. Chem. B* **2004**, *108*, 3377.
[48] Z. R. R. Tian, J. A. Voigt, J. Liu, B. McKenzie, H. F. Xu, *J. Am. Chem. Soc.* **2003**, *125*, 12384.
[49] H. Imai, Y. Takei, K. Shimizu, M. Matsuda, H. Hirashima, *J. Mater. Chem.* **1999**, *9*, 2971.
[50] S. P. Albu, A. Ghicov, J. M. Macak, R. Hahn, P. Schmuki, *Nano Lett.* **2007**, *7*, 1286.
[51] F. Cesano, D. Scarano, S. Bertarione, F. Bonino, A. Damin, S. Bordiga, C. Prestipino, C. Lamberti, A. Zecchina, *J. Photochem. Photobiol. A: Chem.* **2008**, *196*, 143.
[52] J. Robertson, *Mater. Sci. Eng. R: Rep.* **2002**, *37*, 129.
[53] F. Cesano, S. Bertarione, D. Scarano, A. Zecchina, *Chem. Mat.* **2005**, *17*, 5119.
[54] D. Scarano, S. Bertarione, F. Cesano, G. Spoto, A. Zecchina, *Surf. Sci.* **2004**, *570*, 155.
[55] A. Riss, T. Berger, H. Grothe, J. Bernardi, O. Diwald, E. Knozinger, *Nano Lett.* **2007**, *7*, 433.
[56] R. Z. Ma, K. Fukuda, T. Sasaki, M. Osada, Y. Bando, *J. Phys. Chem. B* **2005**, *109*, 6210.
[57] R. A. Zarate, S. Fuentes, J. P. Wiff, V. M. Fuenzalida, A. L. Cabrera, *J. Phys. Chem. Solids* **2007**, *68*, 628.
[58] G. Wu, T. Nishikawa, B. Ohtani, A. Chen, *Chem. Mater.* **2007**, *19*, 4530.
[59] S. Shammugam, A. Gabashvili, D. S. Jacob, J. C. Yu, A. Gedanken, *Chem. Mater.* **2006**, *18*, 2275.
[60] F. Bonino, A. Damin, S. Bordiga, C. Lamberti, A. Zecchina, *Langmuir* **2003**, *19*, 2155.